

ARTICLE OPEN



Curvature-controlled band alignment transition in 1D van der Waals heterostructures

Shu Zhao^{1,2,3}, Chunxia Yang^{2,3}, Ziye Zhu^{2,3}, Xiaoping Yao^{2,3} and Wenbin Li^{1,2,3}✉

The effect of curvature on the band alignment of one-dimensional (1D) van der Waals (vdW) transition metal dichalcogenide (TMDC) heterostructures is studied by comprehensive first-principles calculations. We find that, as the diameter of a TMDC nanotube decreases, the combined effect of curvature-induced flexoelectricity and circumferential tensile strain causes a rapid lowering of the conduction band minimum, whereas the valence band maximum exhibits an initial lowering before rising. As individual TMDC nanotubes form coaxial heterostructures, the concerted effect of diameter-dependent band-edge levels and intertube coupling via flexovoltage can result in a transition of intertube band alignment from Type II to Type I in multiple heterostructural systems, including large-diameter $\text{MoSe}_2@\text{WS}_2$, $\text{MoTe}_2@\text{MoSe}_2$, and $\text{MoTe}_2@\text{WS}_2$ heterostructures. These results lay down a foundation for the rational design of 1D vdW heterostructures.

npj Computational Materials (2023) 9:92; <https://doi.org/10.1038/s41524-023-01052-1>

INTRODUCTION

Band energy alignment is a core concept in the study of semiconductors that explains a wide range of phenomena underlying applications such as transistors and quantum well lasers^{1,2}. The key ingredients for determining the band alignment at a semiconductor interface include the energy levels of the valence band maximum (VBM) and conduction band minimum (CBM) of each semiconductor, as well as possible interfacial coupling effects. In addition to successes in studying bulk semiconductor interfaces, band alignment has demonstrated its predictive power in the study of low-dimensional semiconductor heterostructures such as stacked two-dimensional (2D) materials³, where interlayer excitons were observed in van der Waals (vdW) heterostructures of 2D transition metal dichalcogenides (TMDCs) with a staggered (Type II) band alignment^{4–6}. Recently, one-dimensional (1D) vdW heterostructures of coaxial nanotubes have emerged as an intriguing new class of nanomaterials^{7–12}. Single-walled, single-crystal MoS_2 nanotubes with diameters as small as 3.9 nm have been grown on single-walled carbon nanotubes (SWCNTs) and boron-nitride (BN) nanotubes using chemical vapor deposition⁷. This provides a fresh ground for discovering unique phenomena and functionalities in these novel heterostructures. Understanding the band alignment between coaxial nanotubes in 1D vdW heterostructures will be a critical step in this endeavor.

In this article, we study the band alignment in 1D vdW heterostructures of semiconducting Mo- and W-based TMDC nanotubes. An example of such heterostructures, a WS_2 nanotube nested inside a MoS_2 nanotube, is illustrated in Fig. 1a. Three types of band alignment are possible in such systems: Type I, Type II, and Type III, as shown in Fig. 1b. In Type I band alignment, both the VBM and CBM of the heterostructure reside in the nanotube of narrower bandgap. Electrons and holes excited in the wider bandgap nanotube will both transfer to the narrower bandgap nanotube. The resulting quantum confinement of the carriers within the same region will enhance their radiative recombination. Thus, Type I heterostructures are desirable for light-emitting

applications such as semiconductor lasers and light-emitting diodes¹. In Type II band alignment, the VBM and CBM of the heterostructure reside on different nanotubes, resulting in spatially separated electron-hole pairs. This attribute renders Type II band alignment advantageous in photovoltaic and photodetection applications¹³.

Mo- and W-based TMDC monolayers in 2D vdW heterostructures usually have Type II band alignment (except for $\text{MoTe}_2/\text{WSe}_2$)^{4,5,14,15}. However, our first-principles studies reveal that, in 1D vdW heterostructures with intertube distances similar to the interlayer distances in the corresponding 2D vdW heterostructures, $\text{WS}_2@\text{MoS}_2$ hetero-nanotubes can exhibit Type I band alignment when the diameter of the outer MoS_2 nanotube is below ~3.5 nm. The transition from Type II to Type I band-alignment can also occur in $\text{MoSe}_2@\text{WS}_2$, $\text{MoTe}_2@\text{MoSe}_2$, and $\text{MoTe}_2@\text{WS}_2$ hetero-nanotubes, with even larger critical outer-tube diameters of ~5 nm or above. This transition arises from the combined effect of diameter-dependent band-edge levels of TMDC nanotubes and curvature-induced flexoelectricity that generates strong flexovoltages inside TMDC nanotubes. The ability to control the band alignment types in these 1D vdW heterostructures makes them promising for integrating light-emitting, photodetecting, and photovoltaic applications in a single heterostructural platform.

RESULTS AND DISCUSSION

Diameter-dependent band-edge levels of TMDC nanotubes

To determine the band alignment of 1D vdW heterostructures, we first study the diameter-dependent evolution of the band-edge levels of individual TMDC nanotubes, whose systematic understanding is lacking^{16–25}. The semiconducting Mo- and W-dichalcogenide nanotubes include MoS_2 , MoSe_2 , MoTe_2 , WS_2 , and WSe_2 (the remaining member in this material class, namely WTe_2 , has a semi-metallic ground state²⁶). Our density functional

¹School of Materials Science and Engineering, Zhejiang University, 310027 Hangzhou, China. ²Key Laboratory of 3D Micro/Nano Fabrication and Characterization of Zhejiang Province, School of Engineering, Westlake University, 310030 Hangzhou, China. ³Institute of Advanced Technology, Westlake Institute for Advanced Study, 310024 Hangzhou, China. ✉email: liwenbin@westlake.edu.cn

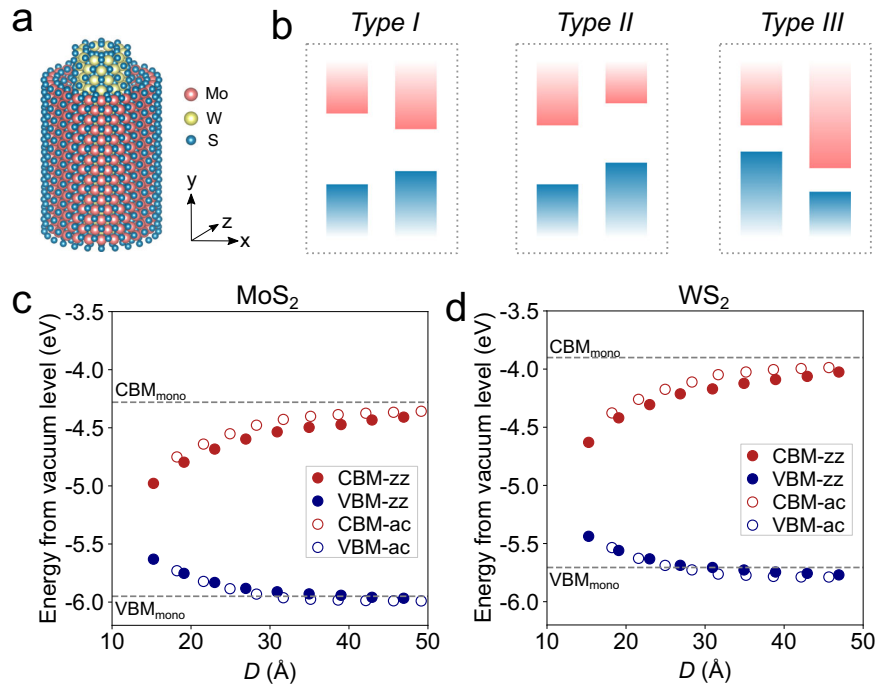


Fig. 1 One-dimensional (1D) van der Waals (vdW) heterostructures and diameter-dependent band-edge levels of MoS_2 and WS_2 nanotubes. **a** Atomistic model of a $\text{WS}_2@\text{MoS}_2$ 1D vdW heterostructure, which corresponds to a smaller-diameter WS_2 nanotube nested in a larger-diameter MoS_2 nanotube. **b** Three types of band alignment in semiconductor heterostructures: Type I (straddling), Type II (staggered), and Type III (broken-gap). **c, d** Band-edge energy levels of MoS_2 nanotubes (**c**) and WS_2 nanotubes (**d**) as a function of tube diameter (D), calculated using density functional theory (DFT). The energies are measured from the vacuum level. The conduction band minimum (CBM) and valence band maximum (VBM) levels of zigzag (zz) and armchair (ac) nanotubes are represented by CBM-*zz*, VBM-*zz*, CBM-*ac*, and VBM-*ac*, respectively. The gray dashed lines illustrate the DFT-calculated CBM and VBM levels of monolayer systems.

theory (DFT) calculations focus on zigzag and armchair nanotubes with diameters ranging from 1.5 nm to 5 nm.

The CBM and VBM levels of MoS_2 and WS_2 nanotubes are presented in Fig. 1c, d. The results reveal that the CBM levels of MoS_2 nanotubes exhibit a continuous lowering with the decrease of tube diameter (as measured from the transition-metal atoms). In contrast, the VBM levels exhibit a more complex change. In the limit of infinitely large diameter, the tube curvature approaches zero and therefore the VBM level shall be equal to that of the corresponding monolayer. However, the VBM levels computed for MoS_2 and WS_2 nanotubes with diameters around 50 Å are still lower than those of the corresponding monolayers, indicating an initial lowering of the VBM levels as the tube diameters decrease. We have verified that this behavior does not come from a numerical convergence issue. The VBM of MoS_2 nanotubes already starts to show a slowly upward shift when the diameter is below ~ 50 Å, whereas in WS_2 nanotubes, the upward shift becomes noticeable at a diameter of ~ 40 Å. When the tube diameter is below 30 Å, the CBM level lowers rapidly with a further reduction of the tube diameter, whereas the VBM level exhibits the opposite trend, rising in a fast pace with decreasing tube diameter. These trends are the same for both zigzag and armchair tubes, indicating a weak chirality dependence of the band-edge level evolution.

The general trend of the variation in the VBM and CBM levels of MoSe_2 , WSe_2 , and MoTe_2 nanotubes are similar to MoS_2 and WS_2 , but the non-monotonic change of their VBM is even more evident, as shown in Fig. 2a–c. Notably, the VBM of the three Se- and Te-based TMDC nanotubes do not rise until the tube diameter is below ~ 30 Å. The transition diameters are ~ 30 Å, 28 Å, and 30 Å for MoSe_2 , WSe_2 , and MoTe_2 nanotubes, respectively. The maximum lowering of the VBM in reference to the corresponding monolayers, reached at the ‘transition diameters’, are on the order of 0.2 eV.

Since VBM and CBM correspond to the edges of the valence and conduction bands, respectively, it is informative to inspect the electronic band structures of TMDC nanotubes. The atomistic structures of zigzag and armchair nanotubes are illustrated in Fig. 2d. The calculated electronic band structures of a zigzag MoSe_2 nanotube with a diameter $D = 41$ Å and an armchair MoSe_2 nanotube of $D = 44$ Å are shown in Fig. 2e, f. At these diameter values, both zigzag and armchair MoSe_2 nanotubes are direct bandgap semiconductors. In the zigzag MoSe_2 nanotubes, both the VBM and CBM reside at the Γ point, whereas in the armchair nanotubes, the band edges are located at around 2/3 of the path from Γ to X , where X is the 1D Brillouin zone boundary. DFT-calculated results indicate that, as the tube diameters are reduced further, zigzag nanotubes will remain their direct-bandgap nature. By contrast, a direct-to-indirect bandgap transition will occur in armchair nanotubes, due to the relative upward shift of the electronic states near Γ (Supplementary Fig. 1). The direct-to-indirect bandgap transition^{25,27} is observed in all armchair nanotubes of Mo- and W-dichalcogenides (MoS_2 , MoSe_2 , MoTe_2 , WS_2 , and WSe_2).

To investigate the origin of the diameter-dependent band-edge levels of TMDC nanotubes, we note that when a TMDC monolayer is wrapped into a nanotube, three distinct factors could affect the band-edge levels: (i) The electron orbitals are spatially confined along the circumferential direction due to the small tube diameter, leading to possible quantum confinement effect (QCE). (ii) The radial curvature of the nanotube can generate flexoelectricity and flexoelectric potential^{28–30} inside the nanotube, which could shift the energy levels of the electronic states. (iii) The bending of a 2D sheet into a nanotube and the subsequent structural relaxation alter the crystal symmetry and generate internal tensile and bending strains in the nanotube, which changes the electron orbital hybridization and thus the band-edge levels. Using a 2D-to-1D band-structure mapping

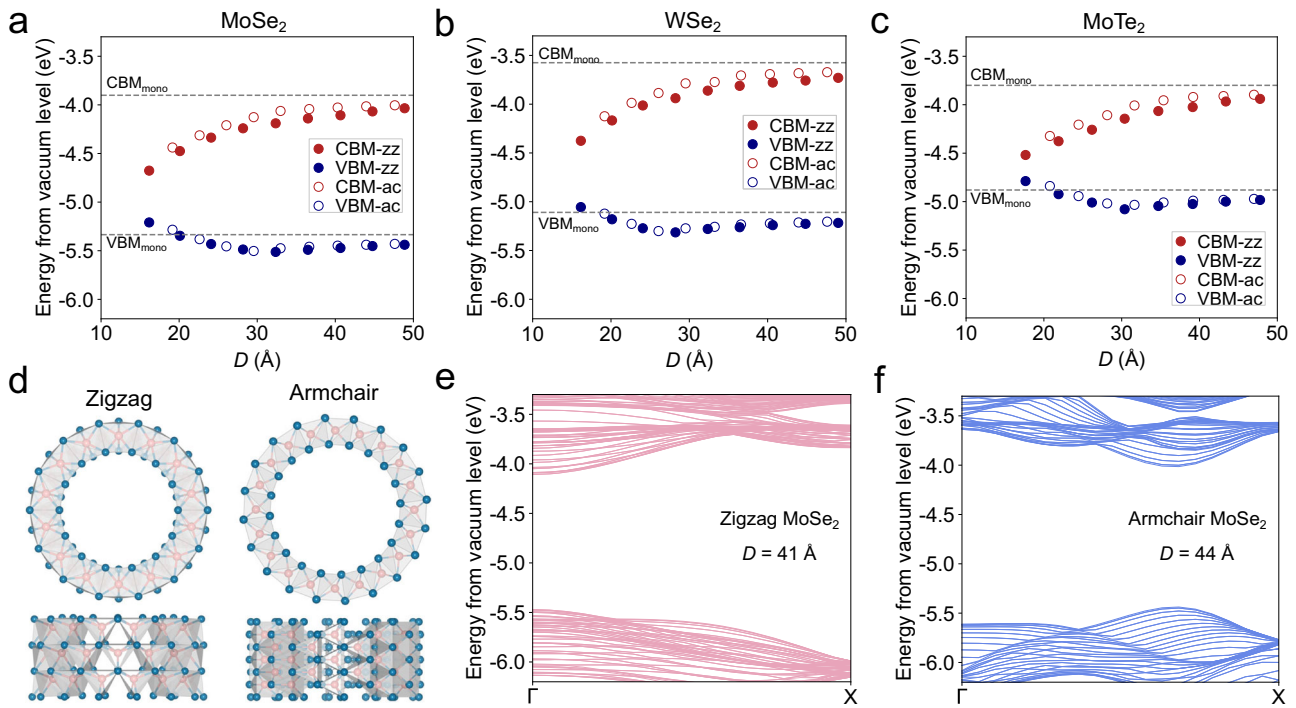


Fig. 2 Diameter-dependent band-edge levels of MoSe₂, WSe₂ and MoTe₂ nanotubes. **a–c** Evolution of the VBM and CBM of MoSe₂, WSe₂, and MoTe₂ nanotubes as a function of tube diameters. **d** Atomistic representations of zigzag and armchair nanotubes of transition metal dichalcogenides (TMDCs), viewed along the tube axis (top panels) and from the side (bottom panels). The pink and cyan spheres represent transition-metal and chalcogen atoms, respectively. **e, f** Electronic band structures of zigzag (**e**) and armchair (**f**) nanotubes with a diameter ~ 40 Å. The electron wave vectors are along the direction of tube axis, and only half of the 1D Brillouin zone is shown due to symmetry.

scheme that was originally developed for the study of QCE in SWCNTs³¹, we find that QCE has a negligible effect on the band-edge levels of TMDC nanotubes (Supplementary Note 1). Hence, our study focuses on the effect of curvature-induced flexoelectricity, circumferential tensile strain, and bending strain on the VBM and CBM levels of TMDC nanotubes.

Curvature-induced flexoelectric and electrostatic potential effect

When a sheet of 2D material is rolled to form a nanotube, the resulting curvature leads to the redistribution of charge inside and outside the nanotube, generating radial electric polarizations^{29,30,32–39}. The resulting radial flexoelectric polarization generates an electrostatic potential difference between the inner and outer sides of the nanotube, as illustrated for a MoSe₂ zigzag (14, 0) nanotube in Fig. 3a. The voltage difference is named flexovoltage and denoted by ΔV_{flexo} , which can be computed as $\Delta V_{\text{exo}} = V_{\text{inner}} - V_{\text{outer}}$. Here V_{inner} and V_{outer} represent the electrostatic potentials of the hollow region inside the tube and the vacuum region far away from the tube surface, respectively. The average electrostatic potential experienced by an electronic state inside a nanotube, whose normalized electron wavefunction given by $\psi(\mathbf{r})$, can be calculated as $\bar{V}_{\text{elstat}} = \int V_{\text{elstat}}(\mathbf{r})|\psi(\mathbf{r})|^2 d\mathbf{r}$. Since the band-edge states of TMDC monolayers and nanotubes predominantly derive from the d orbitals of the transition-metal atoms^{40–42}, the change in \bar{V}_{elstat} of a band-edge state before and after forming a nanotube, denoted by $\Delta \bar{V}_{\text{elstat}}$, can be approximated by the average local electrostatic potential shift near the transition-metal site (ΔV_{core}). ΔV_{core} is calculated within a spherical region centered at the lattice site, with a radius of ~ 1.2 Å, which is roughly half of the nearest-neighbor distance between Mo and Se. We have also calculated the average of the local electrostatic potential shifts of all atoms in the tube, and find that the difference between the two approaches is

small (with a relative difference of $< 10\%$), indicating the validity of our approach. The corresponding electrostatic potential energy shift, $\Delta E_{\text{core}} = -|e|\Delta V_{\text{core}}$, is similar in magnitude to the energy level shift of the core electrons in the transition-metal atoms.

Figure 3b shows the calculated values of ΔV_{core} , together with the values of ΔV_{flexo} for MoSe₂ zigzag nanotubes as a function of inverse diameter $1/D$. The calculated ΔV_{flexo} and ΔV_{core} of MoS₂, WS₂, WSe₂, and MoTe₂ nanotubes are of similar values, as shown in Supplementary Fig. 2. For TMDC tubes with diameters between 50 Å to 15 Å, ΔV_{flexo} are in the range from 0.2 V to 0.4 V, which are three to four times larger than those of SWCNTs at similar diameters³⁰, indicating rather strong flexoelectric effects in TMDC nanotubes. ΔV_{core} is around one half of ΔV_{flexo} at the corresponding diameter. This is understandable given that flexoelectricity-induced electrostatic potential change decreases from the inner to outer side of a tube, eventually becoming zero far outside the tube.

With the calculated electrostatic potential change, we can determine the contribution of curvature-induced flexoelectricity on the band-edge levels of TMDC nanotubes by adding the calculated electrostatic potential energy shift ΔE_{core} to the CBM and VBM energies of the monolayer. The results for MoSe₂ zigzag nanotubes are shown in Fig. 3c. When tube diameters are around or larger than 50 Å, the shifts in the energy levels of the CBM and VBM of MoSe₂ nanotubes with respect to that of the monolayer can be explained by the curvature-induced flexoelectric effect. At smaller diameters (D below 30 Å for VBM and below 50 Å for the CBM of MoSe₂ nanotubes), however, additional contributions beyond flexoelectricity must be taken into account to explain the evolution of band-edge levels.

Circumferential tensile strain effect

When a TMDC monolayer is rolled into a nanotube, the inner layer of chalcogen atoms will be compressed while the outer-layer atoms

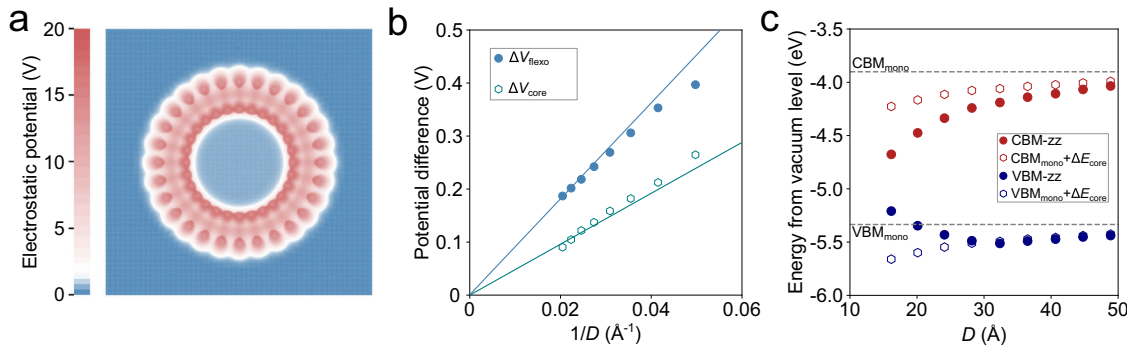


Fig. 3 Effect of curvature-induced flexoelectricity on the band-edge levels of MoSe₂ nanotubes. **a** DFT-calculated electrostatic potential profile in a MoSe₂ (14.0) nanotube. **b** Calculated flexovoltages (filled blue dots) and average local electrostatic potential changes at the Mo site (ΔV_{core} , open green hexagons) as a function of inverse diameter $1/D$. The lines are linear extrapolations of each set of data in the large-diameter limit. **c** Effect of flexoelectricity-induced electrostatic potential energy shift on the band-edge level evolution of MoSe₂ zigzag nanotubes. The filled circles are the VBM and CBM levels of MoSe₂ nanotubes from actual DFT calculations. The open circles represent the model band-edge levels of MoSe₂ nanotubes obtained by adding the VBM/CBM energy levels of MoSe₂ monolayer (VBM_{mono} and CBM_{mono}) with the average electrostatic potential energy shift ($\Delta E_{\text{core}} = -|e|\Delta V_{\text{core}}$, where e is the elementary charge) at the corresponding tube diameter.

are stretched. This causes a distortion to the trigonal prismatic coordination between the transition-metal and chalcogen atoms. The distortion becomes increasingly severe as the tube diameter decreases, resulting in a rapid increase of bending energy⁴³. The bending energy in the system, however, can be partially reduced if the tube diameter is slightly enlarged, albeit at the cost of adding circumferential tensile strain energy into the system.

The competition between bending energy (which favors a larger tube diameter) and circumferential tensile strain energy (which favors a smaller deviation from the original tube diameter) results in an optimized diameter (D) that is slightly larger than the original value (D_0). The circumferential tensile strain ε is defined as the relative change in the circumference of a tube before and after structural relaxation: $\varepsilon = (\pi D - \pi D_0)/\pi D_0$, that is, $\varepsilon = D/D_0 - 1$. Both D and D_0 are measured from the transition-metal atoms. As shown in Fig. 4a, a rapid increase in ε when D is below 50 Å can be observed. The strain versus diameter curve in Fig. 4a can be well fitted by $\varepsilon = a(d/D)^2 + b(d/D)^3$, where $d = 6.5$ Å is the interlayer distance in bulk MoSe₂⁴⁴, and $a = 0.39$, $b = 3.0$ are best-fit numerical coefficients.

The above scaling of circumferential tensile strain ε with respect to the tube diameter D can be rationalized within the framework of continuum mechanics. For a rectangular sheet of solid, after being rolled and ‘weld’ into a tube, its total energy shift E_{total} after structural relaxation is the sum of bending energy E_{bending} and circumferential tensile strain energy E_{tensile} : $E_{\text{bending}} = \frac{1}{6}Y(d/D)^2$, and $E_{\text{tensile}} = \frac{1}{2}Y\varepsilon^2$, where Y is the in-plane Young’s modulus, and d is the thickness of TMDC monolayers⁴⁵. Minimizing E_{total} with respect to D , we obtain the circumferential tensile strain $\varepsilon = \frac{d^2 D_0}{3 D^3} \approx \frac{1}{3} \left(\frac{d}{D}\right)^2$. The coefficient of the second-order term in d/D of the ε versus D scaling from this simple analysis is 1/3, in close agreement with our earlier DFT numerical result of $a = 0.39$.

The above results establish that both circumferential tensile strain and bending strain exist in TMDC nanotubes. The effect of circumferential tensile strain on the band-edge levels of TMDC nanotubes can be studied by looking at the evolution of the band-edge levels of TMDC monolayers under uniaxial tensile strain, and then employing the zone-folding framework developed for QCE (see Supplementary Note 1) to deduce the corresponding changes to the band-edge levels of nanotubes.

We again use MoSe₂ monolayers and nanotubes to illustrate the effect of circumferential tensile strain on band-edge evolutions. Figure 4b, c show that, as uniaxial tensile strain is imposed along the zigzag direction of monolayer, both the absolute energy levels of VBM and CBM at the K point of 2D Brillouin zone exhibit a downward shift, while the VBM at Γ point exhibits an upward shift. This

phenomenon is due to the competition between strain-dependent on-site orbital energy and inter-site orbital hopping energy (see Supplementary Note 2). When the uniaxial tensile strain imposed on a MoSe₂ monolayer is beyond a critical value (~4.9%), the energy of VBM at Γ becomes higher than that of VBM at K , resulting in a direct-to-indirect bandgap transition (Fig. 4c). Since the VBM at K mainly derives from the in-plane transition-metal $d_{x^2-y^2} + d_{xy}$ and chalcogen $p_x + p_y$ orbitals, whereas the VBM at Γ has an out-of-plane transition-metal d_{z^2} and chalcogen p_z character^{40,41}, a transition in the orbital character of the topmost VB state occurs simultaneously. Similar evolution of band-edge states occurs in other strained TMDCs monolayers, and the critical strain of bandgap and orbital character transitions increases in the order of MoS₂, WS₂, MoSe₂, WSe₂, and MoTe₂. This order is mainly due to the larger K - Γ energy separations in the valence bands of selenide monolayers than those in the sulfide counterparts, as the slopes of strain-dependent VBM energies are quite similar among different TMDC monolayers^{46–49}.

On the basis of tensile-strain induced band-edge evolution in TMDC monolayers, we can invoke the monolayer-to-tube electronic structure mapping to understand the effect of circumferential tensile strain on the band-edge states of TMDC nanotubes. For armchair nanotubes, since the 2D electronic states at Γ and K are mapped to different positions in the 1D Brillouin zone of nanotubes (Supplementary Note 1), circumferential tensile strain can cause a direct-to-indirect bandgap transition. For zigzag nanotubes, the 2D states at both Γ and K are mapped to the Γ point of the 1D Brillouin zone. Therefore, although zigzag nanotubes remain direct-bandgap semiconductors¹⁶, a transition in the VBM orbital character from in-plane transition-metal $d_{x^2-y^2} + d_{xy}$ to out-of-plane d_{z^2} orbital will occur when the tube diameter is below a critical value, as shown in Fig. 4d. In Fig. 4e, we further track the energies of topmost in-plane and out-of-plane VB orbitals as a function of tube diameter in MoSe₂ zigzag nanotubes, and find good agreement between the results from 2D-to-1D band folding and actual DFT calculations.

The above results allow us to quantitatively investigate the diameter-dependent band-edge shifts of TMDC nanotubes by taking into account both flexoelectric effect and circumferential tensile strain effect. We model the VBM energy levels of nanotubes as $VBM_{\text{tube}} = VBM_{\text{mono}} + \Delta E_{\text{core}} + \Delta E_{\text{bonding}}$, where VBM_{tube} and VBM_{mono} represent the VBM energies of nanotube and monolayer, respectively. $\Delta E_{\text{bonding}}$ represents the contribution of circumferential tensile strain to band-edge shifting, where only the bonding part of the contribution is included to avoid double counting of the electrostatic contribution, since the latter is

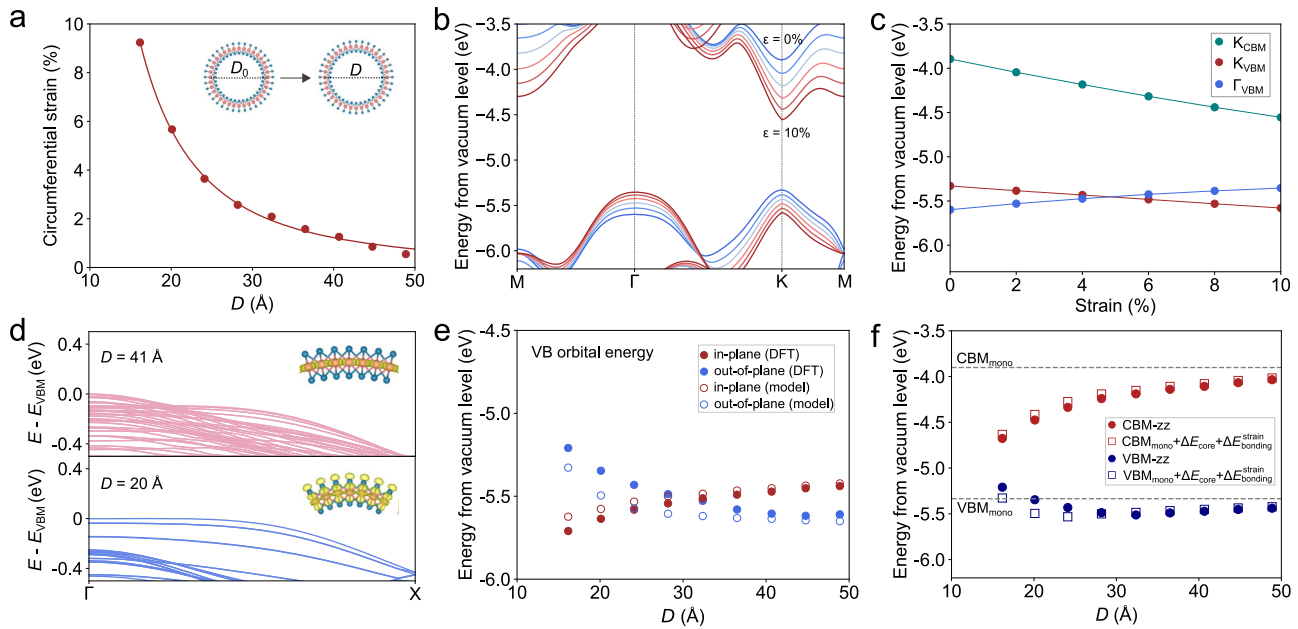


Fig. 4 Effect of circumferential tensile strain on the band-edge levels of MoSe₂ nanotubes. **a** DFT-computed circumferential tensile strain as a function of tube diameter D . The reference for the strain calculation at each tube diameter is the circumference of a corresponding unrelaxed tube rolled from a monolayer. The circumference of a tube is measured from the transition-metal atoms. As illustrated, after structural relaxation $D > D_0$, where D_0 is the original tube diameter. **b** Evolution of the electronic band structure of a MoSe₂ monolayer as a function of uniaxial tensile strain. The strain varies from zero to 10% at a step of 2%. **c** Plot of the band-edge energy levels of MoSe₂ monolayer as a function of uniaxial tensile strain. The green, red, and blue lines represent the data for CBM at K , VBM at K , and VBM at Γ , respectively. **d** Change in the VBM orbital character as the diameter of zigzag MoSe₂ tubes is decreased. The top and bottom panels show the electronic band structures near the VBM of zigzag MoSe₂ tubes with a diameter of 41 Å and 21 Å, respectively. The insets illustrate the electron density isosurface of the corresponding VBM state at Γ . **e** Diameter dependence of the valence-band (VB) orbital energy, for the topmost in-plane and out-of-plane orbitals. The filled circles are from DFT calculations, whereas the open circles are from our model that takes into account both the flexoelectric and circumferential tensile strain effects. **f** Comparison of the DFT-computed CBM and VBM energies of MoSe₂ zigzag nanotubes (filled circles) with those from our model (open squares).

already reflected in ΔE_{core} , as shown in Supplementary Fig. 3. The model for CBM is analogous. We then calculate and plot the modeled VBM and CBM of MoSe₂ zigzag nanotubes and compare the results to actual DFT-computed values, as shown in Fig. 4f. The results demonstrate that for tube diameter above 30 Å, combining flexoelectric effect and circumferential tensile strain effect can well explain the evolution of the energy levels of both VBM and CBM in MoSe₂ nanotubes. In particular, the rapid upward shifts in VBM energies at small tube diameters are correctly captured.

Bending strain effect beyond flexoelectricity

While our model combining flexoelectric and circumferential tensile strain effects can well explain the evolution of band-edge levels in TMDC nanotubes, it can be seen from Fig. 4f that the model prediction becomes less quantitatively accurate as tube diameter becomes smaller, especially when the tube diameter is below the critical point of transition in VBM orbital character. This is because, our model so far has only considered the contribution of bending strain (curvature) to the band-edge level evolution in terms of the flexoelectric and electrostatic potential effect. However, bending strain can also affect the orbital interactions and hence the VBM and CBM levels. Indeed, when the tube diameter is below the transition diameter, both the VBM and CBM of TMDC nanotubes have mainly transition-metal d_{z^2} characters. At the leading order, curvature will reduce the magnitude of the hopping integral t between d_{z^2} orbitals on adjacent sites as $|t| = |t_0| - \gamma \left(\frac{a}{R}\right)^2$, where γ is a coefficient, a is the distance between two neighboring sites, and R is the tube radius (see Supplementary Note 3 for detailed discussions). A decrease in R will contribute to a decrease in the magnitude of the hopping integral t . Hence, bending strain will contribute further to

decreased bonding-antibonding splitting in small-diameter tubes, leading to additional upward shifts of VBM and downward shifts of CBM, which is consistent with the results in Fig. 4f.

To sum up the preceding discussions, the diameter-dependent band-edge evolution of TMDC nanotubes can be well understood by taking into account the effects of flexoelectricity, circumferential tensile strain, and bending strain-induced changes in orbital interactions.

Band alignment transition in 1D vdW heterostructures of TMDC nanotubes

The above understanding of the band-edge evolution in individual nanotubes lays down the basis for understanding the band alignment in heterostructures of TMDC nanotubes. In a 1D vdW heterostructure of coaxial nanotubes, as a smaller-diameter nanotube is nested inside a larger-diameter one, in addition to the intrinsic band-edge level difference between the two nanotubes, the flexovoltage generated by the outer tube will cause an additional shift of the band energy levels in the inner tube. The diameter-dependent band-edge levels of individual nanotubes, in combination with the flexovoltage effect and possibly additional intertube coupling effect, are expected to cause a significant difference between the band alignment of TMDC nanotubes in a 1D vdW heterostructure versus its 2D counterpart, with the possibility of inducing transitions between different types of band alignment. This intriguing possibility is investigated below.

We first study the band-alignment transition in 1D vdW heterostructures of MoS₂ and WS₂ nanotubes. The almost identical lattice constants of MoS₂ and WS₂ ($a_0 \approx 3.18$ Å) allow us to construct a commensurate unit cell of the heterostructure along the tube-axis direction and perform first-principles calculations. Since zigzag and

armchair nanotubes have very similar diameter-dependent band-edge levels, we focus on the heterostructures formed by zigzag nanotubes with chiral indices $(n, 0)$. Furthermore, we focus on heterostructures with intertube distances similar to those in the corresponding 2D vdW heterostructures, as such heterostructures are more likely to be synthesized experimentally⁷. Three types of intertube stacking configurations, namely AA', AB, and AA are considered, the former two corresponding to the 2H and 3R stacking in bulk TMDCs (Supplementary Fig. 4). By varying the chiral index of the outer nanotube (n_{outer}) in $\text{WS}_2(10,0)@\text{MoS}_2(n_{\text{outer}},0)$ heterostructures and calculating the intertube cohesive energies per formula unit, we find that when the chiral index difference between the inner and outer nanotubes corresponds to $n_{\text{outer}} - n_{\text{inner}} = 12$, the intertube cohesive energy is the largest, regardless of the intertube stacking configurations (Supplementary Fig. 5). The corresponding intertube radius difference of 5.9 Å, measured from the transition-metal atoms, is very close to the interlayer distance of ~6.2 Å in MoS_2/WS_2 vdW heterostructures⁵⁰. According to the criterion, other hetero-nanotube systems investigated have the same chiral index difference.

Figure 5a shows the band-edge levels of $\text{MoS}_2(n_{\text{outer}}, 0)$ nanotubes and $\text{WS}_2(n_{\text{outer}} - 12, 0)$ nanotubes as a function of n_{outer} and D_{outer} , before coaxial 1D vdW heterostructures are formed. Between such individually separated nanotubes of MoS_2 and WS_2 , at large tube diameter D_{outer} , the band alignment type belongs to Type II, in consistent with MoS_2/WS_2 2D vdW heterostructures formed by the stacking of monolayers. As the diameters of both inner and outer nanotubes (determined by n_{outer}) decrease, because the CBM energy level of the smaller-diameter $\text{WS}_2(n_{\text{outer}} - 12, 0)$ nanotube decreases faster with n_{outer} than that of the corresponding larger-diameter $\text{MoS}_2(n_{\text{outer}}, 0)$ nanotube, the band alignment eventually becomes Type I, albeit at a small tube diameter of $D_{\text{outer}} \approx 28 Å.$

However, when the WS_2 and MoS_2 nanotubes form coaxial 1D vdW heterostructures, the positive flexovoltage ΔV_{flexo} of the outer MoS_2 nanotube, generated in the region where the smaller-diameter WS_2 nanotube is nested, will cause an additional lowering of the energy levels of the inner tube, thus accelerating the transition of band alignment from Type II to Type I. This is shown in Fig. 5b, where the combined effects of diameter-dependent band-edge levels and flexovoltage-induced electrostatic potential shifts lead to a transition from Type II to Type I band alignment in the $\text{WS}_2@\text{MoS}_2$ 1D vdW heterostructures at a larger critical diameter of $D_{\text{outer}} \approx 35 Å.$

To confirm the existence of Type II to Type I band alignment transition in $\text{WS}_2@\text{MoS}_2$ 1D vdW heterostructures, we have explicitly calculated the electronic band structure of a $\text{WS}_2(10,0)@\text{MoS}_2(22,0)$ coaxial heterostructure. The calculated band structure of the heterostructural system with AA' intertube stacking is shown in Fig. 5c. The other two stacking configurations, AB and AA, have nearly identical band structures (Supplementary Fig. 6). Projection of the electronic states near the fundamental gap onto the inner and outer nanotubes demonstrates that the predominant contribution to both the VBM and CBM of the heterostructural system stems from the inner $\text{WS}_2(10,0)$ nanotube. This is also explicitly shown in Fig. 5d, where it can be seen that both the VBM and CBM wavefunctions are localized on the inner tube. The results thus confirm the formation of a type Type I band alignment in the heterostructure, in consistent with the prediction in Fig. 5b.

The differences in CBM and VBM levels between the model prediction in Fig. 5b and explicit DFT calculation in Fig. 5c are as small as 0.01 eV and 0.15 eV, respectively, indicating weak intertube electronic coupling beyond the flexovoltage effect. This can be understood as a strong internal flexoelectric electric field along the radial direction exists in such 1D vdW heterostructures, whose magnitude is estimated to be on the order of ΔV_{flexo} divided

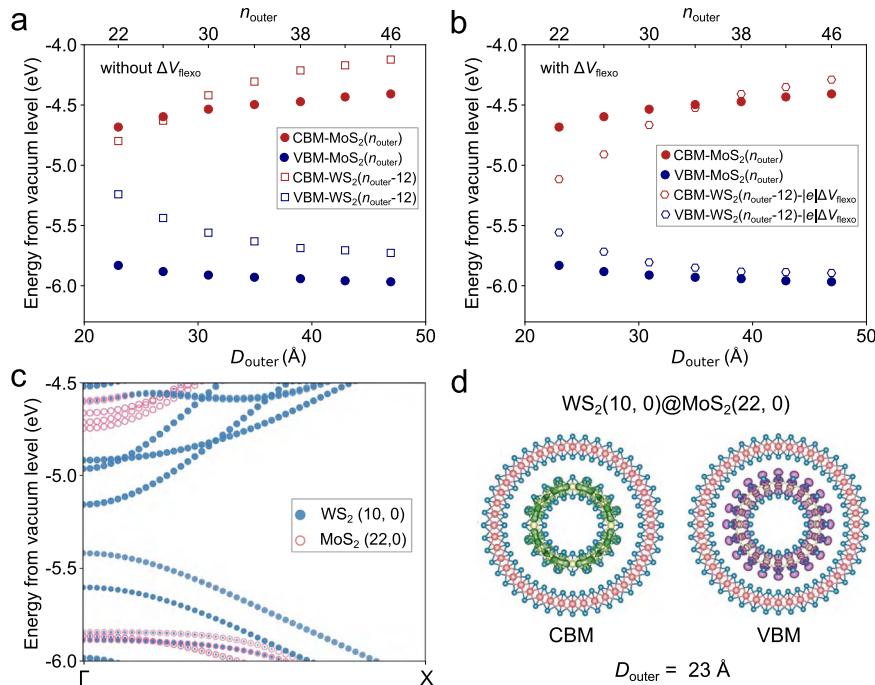


Fig. 5 Band alignment in 1D vdW heterostructures consisting of WS_2 nanotubes nested in MoS_2 nanotubes. **a** CBM and VBM levels of individually separated $\text{MoS}_2(n_{\text{outer}}, 0)$ nanotubes and smaller-diameter $\text{WS}_2(n_{\text{outer}} - 12, 0)$, before forming heterostructures. D_{outer} denotes the diameters of MoS_2 nanotubes in the heterostructures. **b** Alignment of the CBM and VBM levels in $\text{WS}_2@\text{MoS}_2$ 1D vdW heterostructures, after taking into account the flexovoltage effect. The positive flexovoltage that an outer MoS_2 nanotube generates in its interior region leads to a downward shift of the energy levels of the inner WS_2 nanotube by an amount of $-|e|\Delta V_{\text{flexo}}$. **c** Calculated electronic band structure of a $\text{WS}_2(10,0)@\text{MoS}_2(22,0)$ heterostructure. Projection of electronic states to the inner WS_2 nanotube is denoted by blue filled circles and to the outer MoS_2 nanotube by red open circles, with the relative weight represented by the size of the markers. **d** The CBM and VBM wavefunctions (probability density isosurfaces) of the $\text{WS}_2(10,0)@\text{MoS}_2(22,0)$ heterostructure, viewed along the tube-axis direction.

by the thickness of the tube wall (up to 1 V/nm in small-diameter nanotubes), leading to the suppression of intertube electronic coupling^{23,51}.

The computationally proven existence of band alignment transition from Type II to Type I in $WS_2@MoS_2$ 1D vdW heterostructures motivates us to investigate all 20 possible types of 1D vdW heterostructures formed between MoS_2 , $MoSe_2$, $MoTe_2$, WS_2 , and WSe_2 nanotubes. In Supplementary Figs. 7–16, we present the calculated band alignment between $(n_{outer}, 0)$ and $(n_{outer} - 12, 0)$ nanotubes of these TMDCs before and after forming 1D vdW heterostructures, by taking into account the effect of diameter-dependent band-edge levels and flexovoltages. The most important finding from these calculations, as shown in Fig. 6, is that three types of 1D vdW heterostructures, namely $MoSe_2@WS_2$, $MoTe_2@MoSe_2$, and $MoTe_2@WS_2$, exhibit Type I band alignment at large heterostructural tube diameters (D_{outer} around or above 50 Å), which are already experimentally accessible⁷.

The reason that these three 1D vdW heterostructural systems can undergo Type II to Type I band alignment transition at large tube diameters can be understood by considering the band alignment of their corresponding 2D monolayers, which are shown in Fig. 6a. Between any two of $MoSe_2$, $MoTe_2$, and WS_2 monolayers, the difference in their CBM energy levels is small (<0.2 eV), while the difference in their VBM energy levels is relatively large (on the order of 0.5 eV or higher). The small difference in the CBM level of the three TMDCs has been found to be quite robust with respect to the computational methodologies employed¹⁵ (see more discussions in “Methods” section). Thus, although the three TMDCs form Type II band alignment in 2D vdW heterostructures, in 1D vdW heterostructures, if the inner tube belongs to a TMDC that has higher CBM level than the outer TMDC in the monolayer form, due to the combined effect of the inner tube experiencing more diameter-induced lowering of the CBM, as well as the additional lowering of band energies due to

the flexovoltage generated by the outer tube, the CBM level of the inner tube can be pulled down to such a level that it becomes lower than the CBM of the outer tube. Indeed, as can be seen from Supplementary Fig. 2a, the flexovoltages of the TMDC nanotubes, which play a key role in the band alignment transition, still have a large value of 0.15–0.2 eV for tube diameters ~50 Å. In fact, the flexovoltage is a ground state property of the TMDC nanotubes, for which DFT has excellent predictive accuracy. Meanwhile, because the VBM energy difference between the monolayers of inner and outer TMDCs is relatively large, the VBM level of the inner tube remains higher than that of the outer tube. Consequently, a transition from Type II to Type I band alignment is readily induced in these three 1D vdW heterostructure systems.

The existence of Type I band alignment in large-diameter heterostructural systems is important not only because such systems are easier to fabricate experimentally, but also because a large-diameter inner nanotube in the heterostructure would not have undergone a change in the VBM character, therefore still exhibiting strong photoluminescence (Supplementary Note 4). Because these three heterostructural systems have Type I band alignment, electron-hole pairs generated by light illumination on the outer nanotube would be transferred to the inner nanotube region and radiatively recombine and emit photons there, realizing spatially separated photon absorption and emission. As such, these three types of 1D vdW heterostructure ($MoSe_2@WS_2$, $MoTe_2@MoSe_2$, and $MoTe_2@WS_2$) could potentially find important applications in nanoscale optoelectronic devices. The possibility to employ curvature to control the band alignment types in these heterostructural systems could also facilitate the integration of light-emitting, photo-detecting, and photovoltaic functionalities in a single heterostructural material platform.

In conclusion, through comprehensive first-principles calculations and theoretical analysis, we have established a complete framework for understanding the band alignment in 1D vdW heterostructures

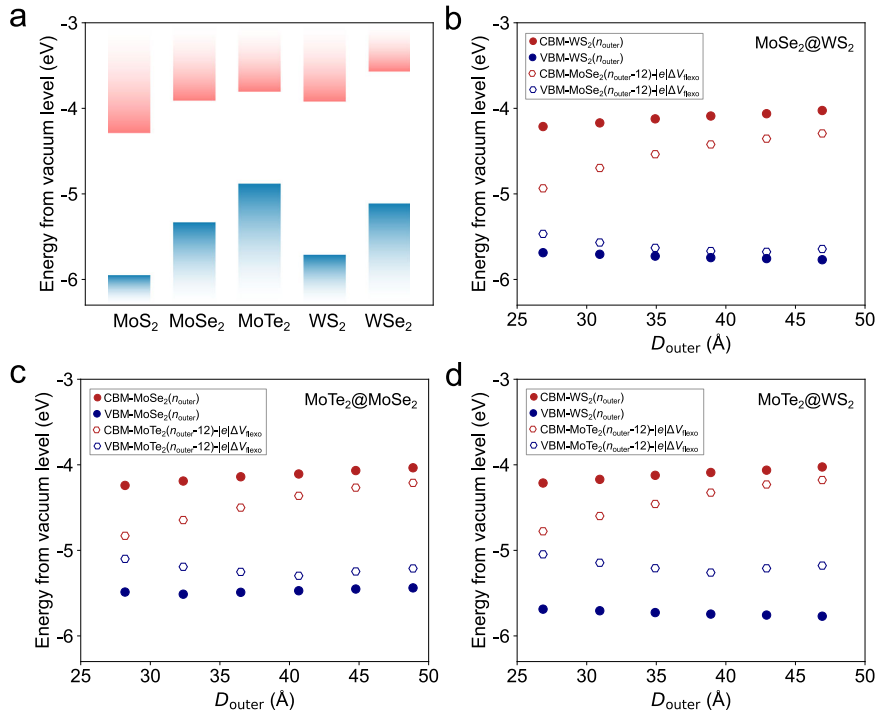


Fig. 6 1D vdW heterostructures that exhibit Type I band alignment at large tube diameters. **a** Calculated band alignment between semiconducting Mo- and W-dichalcogenide monolayers. Blue and red represent valence and conduction band, respectively. **b** Band alignment between inner $MoSe_2$ and outer WS_2 nanotubes in $MoSe_2@WS_2$ 1D vdW heterostructures, constructed from calculated VBM and CBM energy levels of individual $WS_2(n_{outer}, 0)$ and $MoSe_2(n_{outer} - 12, 0)$ nanotubes, and accounting for the additional effect of the flexoelectric potential ΔV_{flexo} generated by the outer WS_2 nanotube on the inner $MoSe_2$ nanotube. **c, d** Similar to **b**, but for $MoTe_2@MoSe_2$ and $MoTe_2@WS_2$ 1D vdW heterostructures, respectively.

of coaxial TMDC nanotubes. We have shown that the CBM levels of individual TMDC nanotubes exhibit a rapid and monotonic lowering when the tube diameter is reduced below 50–60 Å, whereas the VBM of TMDC nanotubes display an initial lowering before rising, with the transition diameter varies from ~50 Å in MoS₂ and WS₂ nanotubes to ~30 Å in MoSe₂, WSe₂, and MoTe₂ nanotubes. These properties can be fully explained in terms of curvature-induced flexoelectricity and the associated electrostatic potential effect, as well as the intrinsic circumferential tensile strain and bending strain within the TMDC nanotubes.

Building on the comprehensive understanding of the diameter-dependent evolution of the band-edge levels in individual TMDC nanotubes, we have investigated the band alignment in all 20 possible types of 1D vdW heterostructures formed between Mo- and W-dichalcogenide nanotubes. We show that the combination of diameter-dependent band-edge levels, as well as the flexovoltage effect, leads to a transition from Type II to Type I band alignment in multiple 1D vdW heterostructural systems. In particular, we identify three 1D vdW heterostructural systems, namely MoSe₂@WS₂, MoTe₂@MoSe₂, and MoTe₂@WS₂, that already exhibit Type II to Type I transition when the outer-tube diameter is around or above 50 Å.

Altogether, our work lays down a key foundation for understanding band alignment in 1D vdW heterostructures and paves the way for rational design of TMDC-based 1D vdW heterostructures.

METHODS

First-principles calculations of the structural and electronic properties of TMDC nanotubes, monolayers, and 1D vdW heterostructures are carried out using DFT within the generalized gradient approximation (GGA) and Perdew-Burke-Ernzerhof (PBE) exchange-correlation functional⁵², as implemented in the Vienna Ab initio Simulation Package (VASP)⁵³. The electron-ion interaction is described using the projector augmented-wave method^{54,55}. Electron wavefunctions are expanded in a plane-wave basis set with a cut-off energy of 350 eV. Atomistic models of TMDC nanotubes are built from TMDC monolayers with fully relaxed lattice constants. To avoid the spurious interaction between periodic image cells in plane-wave DFT calculations, a vacuum space of at least 15 Å perpendicular to the tube-axis direction is added in the supercell, which is sufficient to converge the calculation results. The atomic positions of nanotubes are fully relaxed with force and energy convergence criteria of 0.01 eV/Å and 10⁻⁵ eV, respectively. Given that the difference between the band-edge levels of nanotubes calculated with and without the relaxation of unit-cell dimension along the tube-axis direction is tiny (see the results for MoSe₂ nanotubes in Supplementary Fig. 17), the unit-cell length along the tube-axis direction is fixed in this work. The 2D Brillouin zones of TMDC monolayers are sampled using a 12 × 12 × 1 Monkhorst-Pack mesh, while the 1D Brillouin zones of TMDC nanotubes and heterostructures are sampled using a 1 × 5 × 1 \mathbf{k} -point mesh. The vacuum energy level corresponding to each nanotube, monolayer, or 1D vdW heterostructural system is obtained by calculating the converged Hartree potential energy in the vacuum region far away from the modeled subject. Spin-orbit coupling (SOC) is not included as spin splitting is symmetry forbidden in both zigzag and armchair (non-chiral) nanotubes²¹. We have also compared the electronic band structures of zigzag MoS₂, MoTe₂, and WSe₂ nanotubes calculated with and without SOC, as shown in Supplementary Fig. 18. The results confirm that the difference between the band-edge levels calculated with and without SOC is insignificant. Intertube vdW interactions are included during the structural relaxation of 1D vdW heterostructures, using the DFT-D3 method⁵⁶.

We note that although DFT tends to underestimate the bandgap of semiconductors, previous *GW* calculations on monolayer TMDCs indicate that the underestimation of bandgap is

relatively uniform across different TMDCs¹⁵. In particular, the relative energy differences of CBM levels among different monolayer TMDCs are changed very little as the calculation method changes from DFT to *GW*. Although the large size of the systems that we focus on precludes the use of the *GW* method, we have carried out hybrid functional calculations of the band gaps of MoS₂ and MoSe₂(*n*, 0) nanotubes, as well as 2D monolayers, using the HSE06 functional^{57,58}. Hybrid functional calculations are known to provide more accurate bandgap values than DFT-PBE calculations, but are computationally much more expensive, which limits our calculations to small-diameter nanotubes. The results of the calculations, shown in Supplementary Fig. 19, demonstrate that the HSE bandgap corrections (~0.4 eV) are nearly uniform across different nanotube diameters as well as TMDC types. This indicates that hybrid functional calculations will lead to the same conclusions as in our present study. The flexovoltage of nanotubes, another parameter that plays a key role in determining the band-alignment transition in 1D vdW heterostructures, is a ground state property that can be accurately captured by DFT, as we have noted in the main text.

DATA AVAILABILITY

The datasets used and/or analyzed during the current study are available from the corresponding author upon request.

CODE AVAILABILITY

The DFT calculations in this work were performed using the VASP code, which is a licensed software package. The detailed information related to the VASP code is available at <http://www.vasp.at>.

Received: 30 December 2022; Accepted: 17 May 2023;

Published online: 31 May 2023

REFERENCES

1. Kroemer, H. Nobel lecture: quasielectric fields and band offsets: teaching electrons new tricks. *Rev. Mod. Phys.* **73**, 783–793 (2001).
2. Sze, S. M. *Semiconductor Devices: Physics and Technology* (John Wiley & Sons, 2008).
3. Geim, A. K. & Grigorieva, I. V. Van der Waals heterostructures. *Nature* **499**, 419–425 (2013).
4. Hong, X. et al. Ultrafast charge transfer in atomically thin MoS₂/WS₂ heterostructures. *Nat. Nanotechnol.* **9**, 682–686 (2014).
5. Rivera, P. et al. Observation of long-lived interlayer excitons in monolayer MoSe₂–WSe₂ heterostructures. *Nat. Commun.* **6**, 6242 (2015).
6. Rivera, P. et al. Interlayer valley excitons in heterobilayers of transition metal dichalcogenides. *Nat. Nanotechnol.* **13**, 1004–1015 (2018).
7. Xiang, R. et al. One-dimensional van der Waals heterostructures. *Science* **367**, 537–542 (2020).
8. Xiang, R. & Maruyama, S. Heteronanotubes: challenges and opportunities. *Small Sci.* **1**, 2000039 (2021).
9. Cambré, S. et al. Nanotube-based 1D heterostructures coupled by van der Waals forces. *Small* **17**, 2102585 (2021).
10. Feng, Y. et al. One-dimensional van der Waals heterojunction diode. *ACS Nano* **15**, 5600–5609 (2021).
11. Zheng, Y. et al. One-dimensional van der Waals heterostructures: Growth mechanism and handedness correlation revealed by nondestructive TEM. *Proc. Natl. Acad. Sci. USA* **118**, e2107295118 (2021).
12. Guo, J., Xiang, R., Cheng, T., Maruyama, S. & Li, Y. One-dimensional van der Waals heterostructures: a perspective. *ACS Nanosci. Au* **2**, 3–11 (2021).
13. Lo, S. S., Mirkovic, T., Chuang, C.-H., Burda, C. & Scholes, G. D. Emergent properties resulting from Type-II band alignment in semiconductor nanoheterostructures. *Adv. Mater.* **23**, 180–197 (2010).
14. Kang, J., Tongay, S., Zhou, J., Li, J. & Wu, J. Band offsets and heterostructures of two-dimensional semiconductors. *Appl. Phys. Lett.* **102**, 012111 (2013).
15. Liang, Y., Huang, S., Soklaski, R. & Yang, L. Quasiparticle band-edge energy and band offsets of monolayer of molybdenum and tungsten chalcogenides. *Appl. Phys. Lett.* **103**, 042106 (2013).

16. Seifert, G., Terrones, H., Terrones, M., Jungnickel, G. & Frauenheim, T. Structure and electronic properties of MoS_2 nanotubes. *Phys. Rev. Lett.* **85**, 146 (2000).
17. Seifert, G., Terrones, H., Terrones, M., Jungnickel, G. & Frauenheim, T. On the electronic structure of WS_2 nanotubes. *Solid State Commun.* **114**, 245–248 (2000).
18. Wu, X., Xu, Z. & Zeng, X. C. Single-walled MoTe_2 nanotubes. *Nano Lett.* **7**, 2987–2992 (2007).
19. Milošević, I. et al. Electronic properties and optical spectra of MoS_2 and WS_2 nanotubes. *Phys. Rev. B* **76**, 233414 (2007).
20. Zibouche, N., Kuc, A. & Heine, T. From layers to nanotubes: transition metal disulfides TMS_2 . *Eur. Phys. J. B* **85**, 49 (2012).
21. Milivojević, M., Dmitrović, S., Damnjanović, M. & Vuković, T. Spin-orbit effects in MoS_2 nanotubes. *J. Phys. Chem. C* **124**, 11141–11149 (2020).
22. Ghosh, S. et al. Cathodoluminescence in single and multiwall WS_2 nanotubes: Evidence for quantum confinement and strain effect. *Appl. Phys. Rev.* **7**, 041401 (2020).
23. Wang, X. et al. A revised mechanism of band gap evolution of TMDC nanotubes and its application to Janus TMDC nanotubes: negative electron and hole compressibility. *J. Mater. Chem. C* **9**, 8920–8929 (2021).
24. Mikkelsen, A. E., Bölle, F. T., Thygesen, K. S., Vegge, T. & Castelli, I. E. Band structure of MoSTe Janus nanotubes. *Phys. Rev. Mater.* **5**, 014002 (2021).
25. Hisama, K., Maruyama, M., Chiashi, S., Maruyama, S. & Okada, S. Indirect-to-direct band gap crossover of single walled MoS_2 nanotubes. *Jpn. J. Appl. Phys.* **60**, 065002 (2021).
26. Wilson, J. A. & Yoffe, A. D. Transition metal dichalcogenides discussion and interpretation of observed optical, electrical and structural properties. *Adv. Phys.* **18**, 193–335 (1969).
27. Wu, H.-H., Meng, Q., Huang, H., Liu, C. T. & Wang, X.-L. Tuning the indirect–direct band gap transition in the $\text{MoS}_{2-x}\text{Se}_x$ armchair nanotube by diameter modulation. *Phys. Chem. Chem. Phys.* **20**, 3608–3613 (2018).
28. Shan, B. & Cho, K. First principles study of work functions of single wall carbon nanotubes. *Phys. Rev. Lett.* **94**, 236602 (2005).
29. Artyukhov, V. I., Gupta, S., Kutana, A. & Yakobson, B. I. Flexoelectricity and charge separation in carbon nanotubes. *Nano Lett.* **20**, 3240–3246 (2020).
30. Springolo, M., Royo, M. & Stengel, M. Direct and converse flexoelectricity in two-dimensional materials. *Phys. Rev. Lett.* **127**, 216801 (2021).
31. Dresselhaus, G., Dresselhaus, M. S. & Saito, R. *Physical Properties of Carbon Nanotubes* (World scientific, 1998).
32. Dumitrić, T., Landis, C. M. & Yakobson, B. I. Curvature-induced polarization in carbon nanoshells. *Chem. Phys. Lett.* **360**, 182–188 (2002).
33. Kvashnin, A. G., Sorokin, P. B. & Yakobson, B. I. Flexoelectricity in carbon nanostructures: nanotubes, fullerenes, and nanocones. *J. Phys. Chem. Lett.* **6**, 2740–2744 (2015).
34. Shi, W., Guo, Y., Zhang, Z. & Guo, W. Flexoelectricity in monolayer transition metal dichalcogenides. *J. Phys. Chem. Lett.* **9**, 6841–6846 (2018).
35. Kumar, S., Codony, D., Arias, I. & Suryanarayana, P. Flexoelectricity in atomic monolayers from first principles. *Nanoscale* **13**, 1600–1607 (2021).
36. Codony, D., Arias, I. & Suryanarayana, P. Transversal flexoelectric coefficient for nanostructures at finite deformations from first principles. *Phys. Rev. Mater.* **5**, I030801 (2021).
37. Bennett, D. Flexoelectric-like radial polarization of single-walled nanotubes from first-principles. *Electron. Struct.* **3**, 015001 (2021).
38. Zheng, J.-D. et al. Flexoelectric effect induced p–n homojunction in monolayer GeSe. *2D Materials* **9**, 035005 (2022).
39. Wang, B., Gu, Y., Zhang, S. & Chen, L.-Q. Flexoelectricity in solids: Progress, challenges, and perspectives. *Prog. Mater. Sci.* **106**, 100570 (2019).
40. Zhu, Z. Y., Cheng, Y. C. & Schwingenschlögl, U. Giant spin-orbit-induced spin splitting in two-dimensional transition-metal dichalcogenide semiconductors. *Phys. Rev. B* **84**, 153402 (2011).
41. Cao, T. et al. Valley-selective circular dichroism of monolayer molybdenum disulfide. *Nat. Commun.* **3**, 887 (2012).
42. Liu, G. B., Shan, W. Y., Yao, Y., Wang, Y. & Di, X. Three-band tight-binding model for monolayers of group-VIB transition metal dichalcogenides. *Phys. Rev.* **88**, 0854331–08543310 (2013).
43. Seifert, G., Köhler, T. & Tenne, R. Stability of metal chalcogenide nanotubes. *J. Phys. Chem. B* **106**, 2497–2501 (2002).
44. Bronsema, K. D., De Boer, J. & Jellinek, F. On the structure of molybdenum diselenide and disulfide. *Z. Anorg. Allg. Chem.* **540**, 15–17 (1986).
45. Landau, L. D. & Lifshitz, E. M. *Theory of Elasticity* (Elsevier, 1986).
46. Johari, P. & Shenoy, V. B. Tuning the electronic properties of semiconducting transition metal dichalcogenides by applying mechanical strains. *ACS Nano* **6**, 5449–5456 (2012).
47. Jin, W. et al. Direct measurement of the thickness-dependent electronic band structure of MoS_2 using angle-resolved photoemission spectroscopy. *Phys. Rev. Lett.* **111**, 106801 (2013).
48. Zhang, Y. et al. Direct observation of the transition from indirect to direct bandgap in atomically thin epitaxial MoSe_2 . *Nat. Nanotechnol.* **9**, 111–115 (2014).
49. Wiktor, J. & Pasquarello, A. Absolute deformation potentials of two-dimensional materials. *Phys. Rev. B* **94**, 245411 (2016).
50. Komsa, H.-P. & Krasheninnikov, A. V. Electronic structures and optical properties of realistic transition metal dichalcogenide heterostructures from first principles. *Phys. Rev. B* **88**, 085318 (2013).
51. Ramasubramaniam, A., Naveh, D. & Towe, E. Tunable band gaps in bilayer transition-metal dichalcogenides. *Phys. Rev. B* **84**, 205325 (2011).
52. Perdew, J. P., Burke, K. & Ernzerhof, M. Generalized gradient approximation made simple. *Phys. Rev. Lett.* **77**, 3865 (1996).
53. Kresse, G. & Furthmüller, J. Efficient iterative schemes for ab initio total-energy calculations using a plane-wave basis set. *Phys. Rev. B* **54**, 11169–11186 (1996).
54. Blöchl, P. E. Projector augmented-wave method. *Phys. Rev. B* **50**, 17953–17979 (1994).
55. Kresse, G. & Joubert, D. From ultrasoft pseudopotentials to the projector augmented-wave method. *Phys. Rev. B* **59**, 1758–1775 (1999).
56. Grimme, S., Antony, J., Ehrlich, S. & Krieg, H. A consistent and accurate ab initio parametrization of density functional dispersion correction (DFT-D) for the 94 elements H–Pu. *J. Chem. Phys.* **132**, 154104 (2010).
57. Heyd, J., Scuseria, G. E. & Ernzerhof, M. Hybrid functionals based on a screened coulomb potential. *J. Chem. Phys.* **118**, 8207–8215 (2003).
58. Kruckau, A. V., Vydrov, O. A., Izmaylov, A. F. & Scuseria, G. E. Influence of the exchange screening parameter on the performance of screened hybrid functionals. *J. Chem. Phys.* **125**, 224106 (2006).

ACKNOWLEDGEMENTS

We gratefully acknowledge the support by NSFC under Project No. 62004172. The work of W.L. is partially supported by Research Center for Industries of the Future at Westlake University under Award No. WU2022C041. The authors thank Drs. C.-M. Dai, J.-Q. Wang, and C. Hu for helpful discussions and the HPC Center of Westlake University for technical assistance.

AUTHOR CONTRIBUTIONS

S.Z. and C.Y. carried out the DFT calculations. S.Z. and W.L. analyzed the data and wrote the paper. C.Y., Z.Z., and X.Y. contributed to data interpretation. W.L. designed and led the project.

COMPETING INTERESTS

The authors declare no competing interests.

ADDITIONAL INFORMATION

Supplementary information The online version contains supplementary material available at <https://doi.org/10.1038/s41524-023-01052-1>.

Correspondence and requests for materials should be addressed to Wenbin Li.

Reprints and permission information is available at <http://www.nature.com/reprints>

Publisher's note Springer Nature remains neutral with regard to jurisdictional claims in published maps and institutional affiliations.



Open Access This article is licensed under a Creative Commons Attribution 4.0 International License, which permits use, sharing, adaptation, distribution and reproduction in any medium or format, as long as you give appropriate credit to the original author(s) and the source, provide a link to the Creative Commons license, and indicate if changes were made. The images or other third party material in this article are included in the article's Creative Commons license, unless indicated otherwise in a credit line to the material. If material is not included in the article's Creative Commons license and your intended use is not permitted by statutory regulation or exceeds the permitted use, you will need to obtain permission directly from the copyright holder. To view a copy of this license, visit <http://creativecommons.org/licenses/by/4.0/>.